Magnetospheric convection electric field dynamics and stormtime particle energization: Case study of the magnetic storm of 4 May 1998

George V. Khazanov

National Space Science and Technology Center, NASA Marshall Space Flight Center, Huntsville, Alabama 35899

Michael W. Liemohn

Space Physics Research Laboratory, University of Michigan, Ann Arbor, Michigan 48109

Tim S. Newman

Computer Science Department, The University of Alabama in Huntsville, Huntsville, Alabama 35899

Mei-Ching Fok

Laboratory for Extraterrestrial Physics, Code 692, NASA Goddard Space Flight Center, Greenbelt, Maryland 20771

Aaron J. Ridley

Space Physics Research Laboratory, University of Michigan, Ann Arbor, Michigan 48109

Abstract

It is shown that narrow channels of high electric field are an effective mechanism for injecting plasma into the inner magnetosphere. Analytical expressions for the electric field cannot produce these channels of intense plasma flow, and thus result in less entry and energization of the plasma sheet into near-Earth space. For the ions, omission of these channels leads to an underprediction of the strength of the stormtime ring current and therefore an underestimation of the geoeffectiveness of the storm event. For the electrons, omission of these channels leads to the inability to create a seed population of 10-100 keV electrons deep in the inner magnetosphere. These electrons can eventually be accelerated into MeV radiation belt particles. To examine this, the May 1-7, 1998 magnetic storm is studied with a plasma transport model by using three different convection electric field models: Volland-Stern, Weimer, and AMIE. It is found that the AMIE model can produce particle fluxes that are several orders of magnitude higher in the L=2-4 range of the inner magnetosphere, even for a similar total cross-tail potential difference.

Keywords

1. Introduction

When an explosive solar flare leads to an interplanetary coronal mass ejection (ICME) directed at the Earth, large disturbances in the geomagnetic environment around the planet ensue (Gosling, 1993). One aspect of the resulting magnetic storm, as it is called, is the formation of an intense torus of current around the Earth. This net-westward-flowing current, peaked a few planetary radii above the surface in the equatorial plane, grows for several hours (perhaps a day) during the passage of the ICME. At some point, usually associated with the peak energy input rate (Wu and Lepping, 2002), this current reaches its maximum level and begins to decline back to its nominal prestorm level. This decay can be rapid or slow, depending on the dynamics of the particles in the magnetosphere and the ionic composition of the current carriers (Hamilton et al., 1988; Takahashi et al., 1990; Kozyra et al., 1998; Liemohn et al., 1999, 2001).

This so-called ring current is formed by charged particles being injected into the inner magnetospheric region due to enhanced convective forces (e.g., Alfvén and Fälthammar, 1963; Lyons and Williams, 1984). Because the magnetic field strength monotonically increases and the field line length monotonically decreases as one moves closer to the Earth, this inward convection leads to particle acceleration. This energization results from conservation of both the first and second adiabatic invariants. As the particles enter the dipole-dominated magnetic field near the Earth, they begin to azimuthally drift according to the gradient, curvature, and magnetization forces. The net azimuthal flow from these drift terms is charge dependent, however, with the ions traveling westward and the electrons eastward around the planet. This differential flow results in a westward current, known as the ring current around the Earth.

The formation of the stormtime ring current has been extensively studied over the years. As computational resources increase, bigger and more sophisticated numerical models describing the flow of particles through near-Earth space have been created, allowing for a closer examination of physics involved in this process. Several large-scale ring current codes exist that are presently being used to increase our understanding of the acceleration of particles in the inner

magnetosphere (see the recent reviews by Wolf and Spiro, 1997; Chen et al., 1997; Daglis and Kozyra, 2002). This includes the identification of partial ring current dominance during the main and early recovery phases, the realization that dayside magnetopause flowout is a major loss process for ring current particles, and a quantitative assessment of the importance of wave-particle interactions on the ion distribution in localized regions (particularly the afternoon sector).

One of the largest uncertainties associated with modeling the injection of the ring current is the description of the large-scale electric field. Created by the interaction of the solar wind magnetic field with the magnetosphere, this field provides the convective force to push the particles into the inner magnetosphere. Its dynamical configuration in this region is still a subject of debate. Until recently, in situ measurements were the only means of diagnosing the magnetospheric particle distribution function. From these particle data, several empirical electric field models have been created, such as that by Nishida (1966) and Brice (1967), Volland (1973) and Stern (1975), and McIlwain (1974, 1986). While satellites such as CRRES have produced statistical compilations of the inner magnetospheric electric field (Rowland and Wygant, 1998), the fields are highly variable (up to 6 mV/m) in the nightside at 2<L<6 for large Kp. Ionospheric observations such as those made by the DMSP satellite (e.g., Burke et al., 1998; Anderson et al., 2001) and ground-based radars (e.g., Foster et al., 1986; Yeh et al., 1991) also show high variability in the subauroral nisghtside during active times. That said, statistical models are still one of the best options for describing the near-Earth electric fields. They have been used both successfully and unsuccessfully to reproduce the observed features of the stormtime ring current (e.g., Chen et al., 1993, 1999; Kozyra et al., 1998, 2002; Jordanova et al., 1998, 2001; and Liemohn et al., 2001, 2002). Only recently (from the IMAGE satellite) have global snapshots of the plasma morphology in the inner magnetosphere been obtained with a quality suitable for detailed, quantitative analysis (Burch et al., 2001), and progress in extracting the electric field from these images is slow.

Because the field lines of the inner magnetosphere pass through the midlatitude ionosphere, the convection patterns here are often useful to help explain the dynamics at the higher altitudes. Using the statistical model of Weimer (1996), Jordanova et al. (2001) showed that this technique produces better comparisons against in situ data than do results using the Volland-Stern electric field model. Another ionospheric convection description is obtained through the assimilative mapping of ionospheric electrodynamics (AMIE) technique (Richmond and Kamide, 1988). This approach uses any available ionospheric data for a given time to produce an instantaneous convection pattern. Boonsiriseth et al. (2001) discussed a semiempirical method of mapping these convection patterns out from the ionosphere into the inner magnetosphere, finding that the AMIE model produces small-scale structures in the potential pattern that are not seen in either the Volland-Stern or Weimer models. However, an additional "penetration" electric field (e.g., Ridley and Liemohn, 2002) must also be included to match the observed electric field magnitudes on the duskside low-L region during storm main phases. Recently, Chen et al. (2003) showed that the AMIE-derived equipotentials concentrate in the evening sector during the main phases of storms, providing a channel for rapid transport of plasma sheet ions into L ~ 3-4 (even L~2 for extremely large events). These studies indicate that even though the cross-magnetospheric potential difference is similar for different models, the morphology of the potential pattern plays a crucial role in the formation of the stormtime ring current.

In this study, several electric field models will be used in conjunction with a ring current transport model to examine the differences in the net acceleration to the particles. By examining not only the electric field patterns in the inner magnetosphere but also the resulting ion and electron energy spectra, it is possible to identify the physical mechanisms behind the energization process. In addition, the consequences of these differences in acceleration will be discussed, revealing the importance of an accurate description of the large-scale electric field in the inner magnetosphere. This study will focus on a particular magnetic storm, that of 4 May 1998. This was a very large storm in which the ring current developed quite rapidly, and so it is

a good candidate for investigating particle energization and flow. It is also a storm that has been previously studied by this group (Khazanov et al., 2002), where the influence of self-consistently calculated ion cyclotron waves were examined (particularly the effects in the late recovery phase). Here, the analysis focuses on the initial development of the ring current. Three different electric field models will be compared: Volland-Stern, Weimer, and AMIE.

2. Model Description

We simulate the hot magnetospheric plasma dynamics by solving the bounce-averaged kinetic equation for the phase space distribution function, Q, of the RC ion species (H^+ and O^+), and electrons

$$\frac{\partial Q_\alpha}{\partial t} + \frac{1}{R_o^2}\frac{\partial}{\partial R_o}\left(R_o^2\left\langle\frac{dR_o}{dt}\right\rangle Q_\alpha\right) + \frac{\partial}{\partial\varphi}\left(\left\langle\frac{d\varphi}{dt}\right\rangle Q_\alpha\right) + \frac{1}{\gamma\sqrt{\gamma^2-1}}\frac{\partial}{\partial E}\left(\gamma\sqrt{\gamma^2-1}\left\langle\frac{dE}{dt}\right\rangle Q_\alpha\right) +$$

$$\frac{1}{f(\mu_o)\mu_o}\frac{\partial}{\partial\mu_o}\left(f(\mu_o)\mu_o\left\langle\frac{d\mu_o}{dt}\right\rangle Q_\alpha\right) = \left\langle\frac{\delta Q_\alpha}{\delta t}\right\rangle_{collis} \qquad \alpha = e, H^+$$

(1)

as a function of position in the magnetic equatorial plane (R_0, φ); kinetic energy and the cosine of the equatorial pitch angle (E, μ_0); and time t. Note that the equation is written in relativistic form, where

$$\gamma = 1 + \frac{E}{mc^2}$$

and all of the coefficients in (1) are converted accordingly. All of the bounce-averaged quantities in (1) are denoted with <…>. On the left-hand side, the bracketed terms are the perpendicular flow speeds, and include all electric and magnetic drifts. These velocities, one for each independent variable in the calculation, will be determined from a number of electric field descriptions, to be discussed below. The $f(\mu_0)$ coefficient is a bounce-averaging term that ranges from 0.74 to 1.38 (Ejiri, 1978). The term on the right-hand side of equation (1) includes losses from charge exchange (only for ions), Coulomb collisions (pitch angle scattering and energy degradation terms), and precipitation at low altitudes (assumed lost at 800 km altitude along each

field line). Each of the drift and loss terms is dependent on spatial location, energy, and pitch angle, and can be different for each species. Charge exchange and atmospheric loss are both treated as attenuation multipliers, while Coulomb collisions are described through an energy advection term (loss only) and a pitch angle diffusion term. The formulations for these processes are the same as those discussed in Jordanova et al. (1996). For the electrons, pitch angle diffusion into the loss cone resulting from interactions with the whistler mode waves in the plasmasphere is taken into account via attenuation factors (Lyons et al., 1972). The source of the particles is flow through the nightside outer simulation domain boundary (12 R_E downtail). Loss through the dayside magnetopause is also taken into account, allowing free outflow of the RC electrons and ions from the simulation domain. For further details about the solution of the kinetic equation (1), please see Jordanova et al. (1996, 1997), Khazanov et al. (1998, 1999), and Liemohn et al. (2001).

In the calculations below, several methods will be used to calculate the electric fields in the inner magnetosphere. One will be the analytical formulation of the Volland-Stern potential (Volland, 1973; Stern, 1975), assuming a shielding factor of 2 (nominal shielding near the Earth) and driven by the 3-hour Kp index (Maynard and Chen, 1975). The pattern is rotated 2 hours of local time westward to better match the large-scale convection patterns of the other two models. Another electric field will be an ionosphere-to-magnetosphere mapping of the Weimer-96 model (Weimer, 1996), driven by upstream solar wind measurements (1-minute time cadence). A final electric field model will be an ionosphere-to-magnetosphere mapping of the AMIE inversion (Richmond and Kamide, 1988) of groundbased (magnetometer and radar) and ionospheric (DMSP satellite) data for this interval (also with a 1-minute time cadence).

Background and boundary conditions are also an important consideration for these simulations. The code uses a Rairden et al. (1986) geocoronal description for the charge exchange coefficients, and a Rasmussen et al. (1993) plasmaspheric model for the Coulomb collision coefficients. A static but disturbed Tsyganenko and Stern (1996) magnetic field is used for these calculations, so the results can focus on the influences of the electric field on the ion

7

and electron distribution functions. All of the runs use kappa distributions applied at the outer simulation boundary (12 R_E downtail) for the source populations of the ions and electrons,

$$j(\mathbf{r}, E) = n(\mathbf{r}) \frac{\Gamma(\kappa + 1)}{(\pi \kappa)^{3/2} \Gamma(\kappa - 1/2)} \left(\frac{1}{2 m_o E_o} \right)^{1/2} \frac{E}{E_o} \left(1 + \frac{E}{\kappa E_o} \right)^{-\kappa - 1} \qquad (2)$$

where the differential number flux j is related to the distribution function by $j=2EQ/m^2$. The coefficients are set by upstream solar wind measurements. A kappa distribution is thought to be reasonable because of the isotropization and acceleration of the plasma by the large amplitude plasma waves and magnetic fluctuations in the tail (e.g., Ma and Summers, 1999).

3. The 1-7 May 1998 Storm

The ICME that hit the magnetosphere on 4 May 1998 was a compound stream of a large magnetic cloud interacting with a trailing high-speed stream. Several studies have examined the solar and heliospheric aspects of this event (Gloeckler et al., 1999; Skoug et al., 1999; Farrugia et al., 2002), and details of the solar wind and interplanetary magnetic field can be found therein. It is actually this stream that hits early on 4 May 1998, after the cloud had passed by geospace on 2-3 May 1998. Figure 1 shows the geophysical response to this activity. The Dst index shown in Figure 1a is an hourly value of the globally-averaged midlatitude magnetic perturbation in the north-south direction. In Figure 1b, Kp is a 3-h cadence global activity index related to the amount of fluctuation in auroral-zone groundbased magnetometer records. See Mayaud (1980) for further information about these indices.

Both of these indices are highly disturbed during the early hours of 4 May 1998. Kp is registered on a quasi-logarithmic scale with a range of 0 to 9, and it reaches 9- (second highest value) for one interval (3-6 UT). The Dst index plummets from an already disturbed value of roughly –62 nT to –205 nT in only 3 hours, indicating the presence of a huge ring current. This index then recovers very quickly and is back up to –125 nT only 5 hours later. Note that during

this fast decay of the ring current, Kp is still elevated, indicating the presence of strong magnetospheric convection.

A useful quantity to consider for each of the three electric field descriptions to be discussed in this study is the total cross-tail potential difference. The basic configuration of the magnetospheric convection pattern is a dawn-to-dusk oriented potential drop (that is, electric field), which drifts the plasma sunward. By finding the maximum and minimum values of the potential, as specified by these various techniques, it is possible to obtain a quantitative assessment of the strength of the flow in the inner magnetosphere. The lower 3 panels of Figure 1 show this cross-tail potential difference for the three field models. It is seen that the Weimer-96 potential difference spikes up to more than 300 kV during the main phase injection early on 4 May 1998. Similarly, the AMIE potential difference also has a peak value at this time of around 250 kV. The Volland-Stern potential drop, however, is much lower, with a peak value of just over 100 kV. This is partly due to the extent of the magnetosphere during this interval, because the Volland-Stern potential is directly proportional to the distance away from Earth. Hence a larger magnetosphere results in a bigger potential difference than would a smaller magnetosphere.

4. Results

This study focuses on the formation of the particle distribution function in the inner magnetosphere assuming various descriptions for the large-scale electric field. As mentioned above, three field models will be used: (1) the Volland-Stern empirical model, driven by the 3-h Kp index (interpolated each time step); (2) the Weimer-96 empirical model, driven by the 1-min cadence solar wind and interplanetary magnetic field data; and (3) the AMIE model, driven by 1-min resolution ground-based magnetometer data.

In order to isolate the effects of the electric field configuration, all three simulations are run with exactly the same initial and boundary conditions for the inner magnetospheric plasma

populations. The source term for the plasma is the nightside plasma sheet, which is defined by equation (2) above with $\kappa=3$ and the parameters n and E_0 specified by the upstream solar wind

$$n(t)\left[cm^{-3}\right] = 0.025 N_{sw}(t-3h) + 0.395$$
$$E_0(t)\left[keV\right] = 0.02 V_{sw}(t-3h) - 3.0$$

(3)

as determined from data (Borovsky et al., 1998; Ebihara and Ejiri, 2000). In (3), the units are cm^{-3} for N_{sw} and km/s for V_{sw}. The initial conditions are those specified by Sheldon and Hamilton (1993) for the quiet ring current.

All of the runs were begun at 00 UT on 1 May 1998 and carried out through the end of 7 May 1998. In this study, only a small portion of these simulation results are examined, namely those around 00 UT on 4 May 1998 when the Dst index plummeted toward its minimum value (that is, during the main phase injection of the stormtime ring current). It is during this period that the most intense electric fields are present in the inner magnetosphere, making it an ideal interval to study the acceleration of plasma in near-Earth space.

4.1. Electric Potentials

Figures 2, 3, and 4 show electric equipotential contour plots in a region around the Earth (± 12 R_E in the x-y plane). The 8 panels of each figure are consecutive hourly snapshots of the convection pattern. Each figure shows the patterns for the 3 electric field descriptions, as listed. These times are during the main phase of the storm on 4 May 1998 (01 UT to 08 UT on that day). Because the electric field is directly proportional to the gradient of these potentials, the relative spacing of the contour lines (drawn every 6 kV) show the relative strength of the electric field as a function of space and time. Note that the corotation electric field has been added to all of these plots. Therefore, the equipotential contour lines are the instantaneous cold-plasma drift trajectories through this region. Higher energy particles will, of course, also have the energy, pitch angle, and charge dependent effect of the magnetic gradient-curvature drift superimposed on these trajectories. Even so, it is useful to examine these plots to understand the flow of the plasma sheet particles into the inner magnetosphere during this event. If the electric field is

10

strong enough, the convective drift can dominate the gradient-curvature drift, even for high-energy ions and electrons. The discussion below will therefore focus on the morphology of the potential patterns, especially on regions of intense electric fields (that is, closely-spaced equipotential contours). Such regions will be places of high-speed plasma motion along these equipotential lines, and so they will be referred to as "flow channels" hereinafter, similar to the Chen et al. (2003) study. In fact, Chen et al. (2003) show drift paths instead of equipotentials for these flow channels in the inner magnetosphere, and so it is useful to compare those results with the ones presented here.

Take a look at Figure 2, which are the patterns for the Volland-Stern electric field description. They all look very similar to each other in their general morphology. The region near the Earth where the corotation potential dominates (a minimum at the Earth, so it is an inward electric field and thus an eastward drift) expands and contracts with the waning and waxing of the cross-tail potential difference of the large-scale convection field (maximum at dawn, so it is a dawn-to-dusk electric field and thus a sunward drift). This is the classic description of magnetospheric convection, with a teardrop shaped separatrix dividing the closed trajectories near the planet and the open trajectories farther away. The cold-plasma drift trajectories preferentially flow around the dawn side of the Earth. In all of these plots, the stagnation point is well defined and always located at about 6 R_E just sunward of dusk (not exactly at dusk because the pattern has been rotated westward slightly).

Now consider Figure 3, containing the patterns for the Weimer-96 electric field description. Even though the same corotation potential has been added to both sets of plots, the Weimer-96 contours are quite a bit different than the Volland-Stern patterns. For one, the stagnation point is rotated toward midnight (post-dusk rather than pre-dusk), and the separatrix is much closer to the Earth. The electric fields, as evidenced by the concentration of equipotential contours in a given region, are also larger beyond the separatrix for this field description. Of particular interest for this study are the intense electric fields in the post-dusk region, where the equipotentials are closely spaced and point right at Earth. This phenomenon, which will be

11

dubbed a flow channel, is clearly seen at hours 76 (04 UT) and 77 (05 UT). While the convective electric fields in the Volland-Stern field never exceed 1 mV/m inside of a 8 R_E radius from Earth, in the Weimer-96 model they are able to reach values of 1.7 mV/m in this flow channel.

In Figure 4 (those for the AMIE electric field description), the convection patterns are even more exotic. Flow channels form and disappear regularly during this interval, with the most intense one at hour 78 (06 UT) directed right along the midnight meridian. Here, electric fields in excess of 3 mV/m exist in a narrow band stretching from the 12 R_E outer boundary of the plot in to the 2 R_E inner boundary of the contour traces. These fields are capable of moving plasma from one end of this channel to the other in less than an hour. That is, with electric and magnetic field strengths of 3 mV/m and 100 nT (a nominal field strength near geosynchronous orbit), respectively, the drift speed is 17 R_E/h. So, even though these channels are short-lived in any specific location (the particular one at hour 78 (06 UT) is not present in the midnight sector at either hour 77 (05 UT) or 79 (07 UT), for instance), they are still capable of injecting massive amounts of plasma into the inner magnetosphere, as will be shown below.

In comparing the cross-tail potential differences given in Figure 1 with the patterns shown in Figure 2, 3 and 4, it is seen that the Weimer-96 model produced the largest cross-tail potential difference while the AMIE model produced the largest electric fields. Because the energization of the plasma is directly related to how far in the plasma is injected into the inner magnetosphere, it is really the electric field that matters for this study. Therefore, while it is useful to consider the cross-tail potential difference as a general indicator of the convective strength at a given time, it is really the morphology of the potential pattern that yields the strong flow channels capable of accelerating the plasma sheet particles up to ring current energies.

4.2. Particle Energy Spectra

To illustrate the effect of these flow channels on the particles, the pitch angle averaged energy spectra of differential number flux will be examined. Figure 5 presents the results for

protons at hour 74 (02 UT), a time near the start of the main phase of the 4 May 1998 storm. Even here, before the main storm, there are significant differences in the flux levels between the various simulations. This is because there was a smaller storm on 2 May 1998 that is still persisting (Dst was still below –50 nT at the start of 4 May 1998). At larger radial distances, the 3 models produce nearly identical spectra because this is essentially the outer boundary condition, particularly true at MLT=00. At smaller radial distances, the differences become clear. The AMIE fields are capable of creating an energetic population deep in the inner magnetosphere (flux peak near 100 keV) that is several orders of magnitude larger than that from the other field models. The peak at the highest energy bin (near 400 keV) in the Volland-Stern and Weimer-96 field results are remnants of the specified initial condition. Very little new protons have been injected, thus far in the storm sequence, by either of these two field models. The AMIE potentials, however, even with modest cross-tail potential differences of under 150 kV, have been able to generate a substantial new ring current inside of 4 R_E. The Weimer-96 fields, even though they have had larger cross-tail potential differences earlier in the sequence, have been able to only generate a small ring current in this region.

Taking these fluxes as a reference point, now consider the fluxes plotted in Figure 6. These are results at hour 80 (08 UT, 6 hours later), after the main phase of the storm (just past the minimum in Dst). The results at L=6.5 and 4.3 are quite similar to those in Figure 5. This is because these radial distances are, in general, on open drift paths even for moderate convection, and thus even the small storm on 2 May 1998 can populate this region with fresh plasma sheet ions. At L=4.3, MLT=16, however, the lower-energy part of the spectra is filled in for the AMIE field results, while the other models still show the standard "accessibility gap" in the spectra. This minimum at a few keV is due to the interplay between the corotation, convective, and gradient-curvature drifts for protons. Corotation is eastward while gradient-curvature is westward (convection is basically sunward). Ions of a few keV have gradient-curvature drifts on the order of the corotation drifts around L=3-5, and so these ions stagnate on the nightside and are slowly lost due to collisional processes (mainly charge exchange and Coulomb interactions).

13

That this minimum is not evident in the AMIE field results indicates that, at some point on the nightside, the convective drift was strong enough to overcome this stagnation and push the ions in toward the Earth.

At smaller L values (3.2 and 2.6), the differences between Figure 6 and Figure 5 become more apparent. At L=3.2, the low-energy range of the spectrum is enhanced for all of the field models at MLT=00 but only for the AMIE field run at MLT=16. The sharp peak near 20 keV at MLT=16 in the Weimer-96 and Volland-Stern field results are from convective access during the main phase. However, it is seen that neither of these models were capable of producing the high-energy population that the AMIE field results show. At L=2.6, the differences between the AMIE results and the other model results are even more dramatic. Again, there is a peak near 30 keV in the Weimer-96 and Volland-Stern field results at MLT=16, but these do not reach the AMIE flux levels, and neither the low nor high energy tails of the spectrum are even close to the AMIE field flux levels. In comparing Figures 5 and 6, it is seen that the AMIE fields during the main phase on 4 May 1998 increased the high-energy flux levels by at least an order of magnitude at the deepest L shells. This energization is primarily due to the rapid injection of plasma sheet ions via the flow channels and their intense electric fields.

A similar analysis can be done for the electron flux spectra. These particles have an eastward gradient-curvature drift, and so this term is in the same sense as corotation. Therefore, stagnation will only occur where these two drifts are equal and opposite to the convective drift, which generally occurs in the dusk sector (if at all). The net influence is that the plasma sheet electrons will all flow eastward during injections, in contrast to ions that might flow either direction, depending on their energy. It is therefore more difficult to inject electrons deep into the inner magnetosphere, especially the high-energy electrons (for which the gradient-curvature drift term is large). A very intense electric field is needed to bring these particles inside of L=4.

Figure 7 shows the electron spectra from the three simulations at hour 74 (02 UT). As with the ions, the L=6.5 fluxes are very similar between the models and are close to the outer boundary flux values. Deeper in L shell and at the sub-100-keV energies, it is seen that the

14

Weimer-96 model produces consistently higher flux levels than the Volland-Stern field simulation. In turn, the AMIE model yields higher flux levels than either of the other two in this range. Again, it is not the total potential difference that determines the flux levels but the maximal localized electric fields that preferentially bring in the plasma sheet electrons to the inner magnetosphere. At the smaller radial distances, the Volland-Stern results are a good indication of the prescribed initial condition values.

Figure 8 shows electron flux results at hour 80 (08 UT), after the main phase of the storm. The changes are subtler than those seen in the ion results, but interesting features should be pointed out. Consider, for instance, L=4.3. Here the Weimer-96 and AMIE potentials yield enhanced fluxes in the high-energy tail of the distribution compared to their prestorm fluxes, while the Volland-Stern model produced almost no change at all (except in the lowest energy channels shown). This difference is from convective access of these particles into the inner magnetosphere. How far in did they penetrate? Examining the results at L=3.2 and L=2.6 shows that the fluxes are either at or slightly below their prestorm values. Therefore, the inward penetration of electrons due to the flow channels was much less critical than that for the ions. Note that, because of differences in the characteristic energy and number density between the hot ions and hot electrons, most of the total energy in the inner magnetosphere is carried by the hot ions rather than the hot electrons, and therefore it is the energization of the ions that plays the vital role in forming a strong stormtime ring current near the Earth. That said, the sub-100-keV electrons that are brought in by these flow channels form the seed population for the radiation belts. Through resonant interactions between plasma waves and the drift period of these electrons, additional acceleration can result, yielding a post-storm radiation belt enhancement, as is often seen (e.g., McIlwain, 1996, and references therein).

4.3. Temporal Evolution

To understand the global morphology differences in the particle distributions resulting from the electric field choices, Figures 9 and 10 present color spectrograms of the pitch-angle

averaged flux at a given energy throughout the inner magnetosphere. The two figures are for ions and electrons, respectively. Each of the plots in Figures 9 and 10 show the results inside of 6.6 R_E (geosynchronous orbit; which is a convenient but somewhat arbitrary boundary for the inner magnetosphere). In addition, local midnight is to the right, dawn is to the top, noon is to the left, and dusk is to the bottom in each plot. There are three sets of 15 plots in Figures 9 and 10. The 15 plots are at 5 times throughout the storm event and at 3 energies. The times are as follows: May 3 at 16 UT (hour 64, before the storm); 4 May 1998 at 02 UT (hour 74, at the start of the main phase); 4 May 1998 at 08 UT (hour 80, just after the storm minimum); 4 May 1998 at 16 UT (hour 88, during the recovery phase); and 5 May 1998 at 00 UT (hour 96, in the late recovery phase). These are chosen to illustrate the temporal evolution of the results before, during, and after the energization process. For the ions (Figure 9), the chosen energies are the computational bins centered at 8 keV, 38 keV, and 106 keV, while for the electrons (Figure 10), the chosen energies are 10 keV, 96 keV, and 297 keV. These are selected to best highlight the differences between the results from the 3 electric field models.

In Figure 9, it is seen that all three field models have comparable fluxes of 8 keV ions in the inner magnetosphere. In fact, the results from the AMIE potential simulation have, in general, lower fluxes than the other two simulations at this energy. It is also seen that the fluxes at this energy are quickly depleted during the recovery phase of the storm. This is due to the fast charge exchange timescale for H^+ ions below 30 keV (e.g., Fok et al., 1991). At higher energies, the differences between the field models become more apparent. For both the 38 keV and the 106 keV results, there is a clear increase of flux intensity from the Volland-Stern potential results to the Weimer-96 potential results to the AMIE potential results. This is especially true at 106 keV, where the AMIE potential was able to form a strong symmetric ring current in the 2-4 R_E range. The 106 keV fluxes from the AMIE potential continue to increase into the recovery phase of the storm due to acceleration of lower-energy particles through resonant interaction with the electric field variations. This shows that the energy spectra shown in Figure 6 are not isolated

examples that best show the differences, but are rather typical examples that fit into a larger pattern of systematic differences between the simulation results.

Figure 10 shows a similar picture for the electron fluxes. For the electrons, a seed population in the 100 keV to 1 MeV range is needed for creation of the radiation belts after storms. Therefore, a desired result is the injection and capture of the plasma sheet electrons into a well-formed electron ring current. The Volland-Stern potential description is incapable of producing a torus of intense electron fluxes in the inner magnetosphere. The Weimer-96 model is better at producing this feature, particularly at injecting electrons inside of 4 R_E. The AMIE model, however, is exceptionally good at creating an intense electron ring current. All three selected energies are higher than the results from the other two electric potential models practically everywhere in the inner magnetosphere. It is clear that the flow channels are responsible for creating this injection and energization of the electrons.

5. Conclusions

It was the goal of this study to present simulation results that show the importance of flow channels into the inner magnetosphere for the formation of the stormtime ring current. These flow channels are very efficient at producing high-energy ions close to the Earth (inside of L=4), and are therefore thought to be a major contributor to the formation of the stormtime ring current. These flow channels, which are regions of densely-packed equipotential lines pointed at the Earth (that is, strong azimuthal electric fields yielding large inward drifts) can wax and wane on the order of an hour. Even still, this is ample time for the convection of particles from the near-Earth plasma sheet into the inner magnetosphere.

A consequence of this is that modeling of the stormtime ring current must include these high-speed channels, or the geoeffectiveness of the storm event will be underestimated. That is, not as many ions will be brought in close to the Earth, and thus the ring current strength will be underpredicted by the simulation. The Volland-Stern model, which has been used extensively in

17

ring current modeling, was shown in this study to be completely incapable of producing flow channels in the electric field distribution.

Another influence of these flow channels is the creation of the seed population for the radiation belts. These flow channels are capable of injecting electrons up to 100 keV deep into the inner magnetosphere. Subsequent wave-particle interactions and acceleration processes can energize these electrons into the MeV range (e.g., Elkington et al., 1999; Summers and Ma, 2000), where they can then damage spacecraft electronics and subsystems through dieletric charging. Without these flow channels, this seed population is not created, and therefore other mechanisms must be contemplated for the creation of the radiation belts after storms. This study shows that a realistic potential pattern that includes intense flow channels can produce the necessary seed population.

References

Alfvén, H., and C.-G. Fälthammar, *Cosmical Electrodynamics*, Oxford University Press, London, 1963.

Anderson, P. C., D. L. Carpenter, K. Tsuruda, T. Mukai, and F. J. Rich, Multisatellite observations of rapid subauroral ion drifts (SAID), *J. Geophys. Res., 106*, 29,585, 2001.

Boonsiriseth, A., R. M. Thorne, G. Lu, V. K. Jordanova, M. F. Thomsen, D. M. Ober, and A. J. Ridley, A semiempirical equatorial mapping of AMIE convection electric potentials (MACEP) for the January 10, 1997, magnetic storm, *J. Geophys. Res., 106*, 12, 903, 2001.

Borovsky, J. E., M. F. Thomsen, and R. C. Elphic, The driving of the plasma sheet by the solar wind, *J. Geophys. Res., 103*, 17,617-17,639, 1998.

Brice, N. M., Bulk motion of the magnetosphere, *J. Geophys. Res., 72*, 1246, 1967.

Burch, J. L., et al., Views of Earth's magnetosphere with the IMAGE satellite, *Science, 291*, 619, 2001.

Burke, W. J., N. C. Maynard, M. P. Hagan, R. A. Wolf, G. R. Wilson, L. C. Gentile, M. S. Gussenhoven, C. Y. Huang, T. W. Garner, and F. J. Rich, Electrodynamics of the inner magnetosphere observed in the dusk sector by CRRES and DMSP during the magnetic storm of June 4-6, 1991, *J. Geophys. Res., 103*, 29,399, 1998.

Chen, M. W., M. Schulz, L. R. Lyons, and D. J. Gorney, Stormtime transport of ring current and radiation belt ions, *J. Geophys. Res., 98*, 3835, 1993.

Chen, M.W., M. Schulz, and L. R. Lyons, Modeling of ring current formation and decay: A review, in *Magnetic Storms, Geophys. Monogr. Ser.*, vol. 98, edited by B. T. Tsurutani, W. D. Gonzalez, Y. Kamide, and J. K. Arballo, American Geophysical Union, Washington, D. C., p. 173, 1997.

Chen, M. W., M. Schulz, G. Lu, and L. R. Lyons, Quasi-steady drift paths in a model magnetosphere with AMIE electric field: Implications for ring current formation, *J. Geophys. Res., 108*(A5), 1180, doi: 10.1029/2002JA009584, 2003.

Chen, M. W., J. L. Roeder, J. F. Fennell, L. R. Lyons, R. L. Lambour, and M. Schulz, Proton ring current pitch angle distributions: Comparison of simulations with CRRES observations, *J. Geophys. Res., 104*, 17,379, 1999.

Daglis, I. A., and J. U. Kozyra, Outstanding issues of ring current dynamics, *J. Atmos. Solar-Terr. Phys., 64*, 253, 2002.

Ebihara, Y., and M. Ejiri, Modeling of solar wind control of the ring current buildup: A case study of the magnetic storms in April 1997, *Geophys. Res. Lett., 25*, 3751, 1998.

Ebihara, Y., and M. Ejiri, Simulation study on fundamental properties of the storm-time ring current, *J. Geophys. Res., 105*, 15,843-15,859,2000.

Ejiri, M., Trajectory traces of charged particles in the magnetosphere, *J. Geophys. Res., 83*, 4798, 1978.

Elkington, S. R., M. K. Hudson, and A. A. Chan, Acceleration of relativistic electrons via drift-resonant interaction with toroidal-mode Pc-5 ULF oscillations, *Geophys. Res. Lett., 26*, 3273, 1999.

Farrugia, C. J., et al., Wind and ACE observations during the great flow of 1-4 May 1998: Relation to solar activity and implications for the magnetosphere, *J. Geophys. Res., 107*(A9), 1240, doi: 10.1029/2001JA000188, 2002.

Fok, M.-C., J. U. Kozyra, A. F. Nagy and T. E. Cravens, Lifetime of ring current particles due to Coulomb collisions in the plasmasphere, *J. Geophys. Res., 96*, 7861-7867, 1991.

Foster, J. C., J. M. Holt, R. G. Musgrove, and D. S. Evans, Ionospheric convection associated with discrete levels of particle precipitation, *Geophys. Res. Lett., 13*, 656, 1986.

Gloeckler, G., et al., Unusual composition of the solar wind in the 2-3 May 1998 CME observed with SWICS on ACE, *Geophys. Res. Lett., 26*, 157, 1999.

Gosling, J. T., The solar flare myth, *J. Geophys. Res., 98*, 18,937, 2001.

Hamilton, D. C., G. Gloeckler, F. M. Ipavich, W. Studemann, B. Wilkey, and G. Kremser, Ring current development during the great geomagnetic storm of February 1986, *J. Geophys. Res., 93*, 14343-55, 1988.

Jordanova, V. K., L. M. Kistler, J. U. Kozyra, G. V. Khazanov, and A. F. Nagy, Collisional losses of ring current ions, *J. Geophys. Res., 101*, 111, 1996.

Jordanova, V. K., J. U. Kozyra, A. F. Nagy, and G. V. Khazanov, Kinetic model of the ring current-atmosphere interactions, *J. Geophys. Res., 102*, 14,279, 1997.

Jordanova, V. K., C. J. Farrugia, L. Janoo, J. M. Quinn, R. B. Torbert, K. W. Ogilvie, R. P. Lepping, J. T. Steinberg, D. J. McComas, R. D. Belian, October 1995 magnetic cloud and accompanying storm activity: ring current evolution, J. Geophys. Res., 103, 79, 1998.

Jordanova, V. K., L. M. Kistler, C. J. Farrugia, and R. B. Torbert, Effects of inner magnetospheric convection on ring current dynamics: March 10-12, 1998, *J. Geophys. Res., 106*, 29,705, 2001.

Khazanov, G. V., M. W. Liemohn, J. U. Kozyra, and T. E. Moore, Global superthermal electron transport: Photoelectron and plasma sheet electron sources, *J. Geophys. Res.*, *103*, 23,485, 1998.

Khazanov, G. V., M. W. Liemohn, E. N. Krivorutsky, J. M. Albert, J. U. Kozyra, and B. E. Gilchrist, Relativistic electron beam propagation in the Earth's magnetosphere, *J. Geophys. Res., 104*, 28,587, 1999.

Khazanov, G. V., K. V. Gamayunov, V. K. Jordanova, and E. N. Krivorutsky, A self-consistent model of the interacting ring current ions and electromagnetic ion cyclotron waves, initial results: Waves and precipitating fluxes, *J. Geophys. Res., 107*, 1085, doi: 10.1029/2001JA000180, 2002.

Kozyra, J. U., M.-C. Fok, E. R. Sanchez, D. S. Evans, D. C. Hamilton, and A. F. Nagy, The role of precipitation losses in producing the rapid early recovery phase of the great magnetic storm of February 1986, *J. Geophys. Res., 103*, 6801, 1998.

Kozyra, J. U., M. W. Liemohn, C. R. Clauer, A. J. Ridley, M. F. Thomsen, J. E. Borovsky, J. L. Roeder, and V. K. Jordanova, Two-step Dst development and ring current composition changes during the 4-6 June 1991 magnetic storm, *J. Geophys. Res.*, 1224, doi: 10.1029/2001JA000023, 2002.

Liemohn, M. W., J. U. Kozyra, V. K. Jordanova, G. V. Khazanov, M. F. Thomsen, and T. E. Cayton, Analysis of early phase ring current recovery mechanisms during geomagnetic storms, *Geophys. Res. Lett., 25*, 2845, 1999.

Liemohn, M. W., J. U. Kozyra, M. F. Thomsen, J. L. Roeder, G. Lu, J. E. Borovsky, and T. E. Cayton, Dominant role of the asymmetric ring current in producing the stormtime Dst*, *J. Geophys. Res., 106*, 10,883, 2001.

Liemohn, M. W., J. U. Kozyra, M. R. Hairston, D. M. Weimer, G. Lu, A. J. Ridley, T. H. Zurbuchen, and R. M. Skoug, Consequences of a saturated convection electric field on the ring current, *Geophys. Res. Lett., 29*(9), 1348, doi: 10.1029/2001GL014270, 2002.

Lyons, L. R., R. M. Thorne, and C. F. Kennel, Pitch-angle diffusion of radiation belt electrons with the plasmasphere, *J. Geophys. Res., 77*, 3455, 1972.

Lyons, L. R., and D. J. Williams, *Quantitative Aspects of Magnetospheric Physics*, D. Reidel, Dordrecht-Holland, 1984.

Ma, C.-Y., and D. Summers, Correction to "Formation of power-law energy spectra in space plasmas by stochastic acceleration due to whistler-mode waves", *Geophys. Res. Lett. 26*, 1121, 1999.

Maynard, N. C., and A. J. Chen, Isolated cold plasma regions: Observations and their relation to possible production mechanisms, *J. Geophys. Res., 80*, 1009, 1975.

Mayaud, P. N., *Derivation, Meaning, and Use of Geomagnetic Indices, Geophys. Monogr. Ser.*, vol. 22, American Geophysical Union, Washington D. C., 1980.

McIlwain, C. E., Substorm injection boundaries, in *Magnetospheric Physics*, ed. B. M. McCormac, p. 143, 1974.

McIlwain, C. E., A Kp dependent equatorial electric field model, *Adv. Space Res., 6(3)*, 187, 1986.

McIlwain, C. E., Processes acting upon outer zone electrons, in *Radiation Belts: Models and Standards, Geophys. Monogr. Ser.*, vol. 97, edited by J. F. Lemaire, D. Heynderickx, and D. N. Baker, American Geophysical Union, Washington, D. C., p. 15, 1996.

Nishida, A., Formation of a plasmapause, or magnetospheric plasma knee by combined action of magnetospheric convection and plasma escape from the tail, *J. Geophys. Res., 71*, 5669, 1966.

Rairden, R. L., L. A. Frank, and J. D. Craven, Geocoronal imaging with Dynamics Explorer, *J. Geophys. Res., 91*, 13,613, 1986.

Rasmussen, C. E., S. M. Guiter, and S. G. Thomas, Two-dimensional model of the plasmasphere: refilling time constants, *Planet. Space Sci., 41*, 35-42, 1993.

Richmond, A. D., and Y. Kamide, Mapping electrodynamic features of the high-latitude ionosphere from localized observations: Technique, *J. Geophys. Res., 93*, 5741, 1988.

Ridley, A. J., and M. W. Liemohn, A model-derived description of the penetration electric field, *J. Geophys. Res., 107*(A8), 1151, doi: 10.1029/2001JA000051, 2002.

Sheldon, R. B., and D. C. Hamilton, Ion transport and loss in the Earth's quiet ring current. 1. Data and standard model, J. Geophys. Res., 98, 13491-13508, 1993.

Skoug, R. M., et al., A prolonged He$^+$ enhancement within a coronal mass ejection in the solar wind, *Geophys. Res. Lett., 26*, 161, 1999.

Stern, D. P., The motion of a proton in the equatorial magnetosphere, *J. Geophys. Res., 80*, 595, 1975.

Summers, D., and C.-Y. Ma, Rapid acceleration of electrons in the magnetosphere by fast-mode MHD waves, *J. Geophys. Res., 105*, 15,887, 2000.

Takahashi, S., T. Iyemori, and M. Takeda, A simulation of the storm-time ring current, *Planet. Space Sci., 38*, 1133, 1990.

Tsyganenko, N. A., and D. P. Stern, Modeling the global magnetic field of the large-scale Birkeland current systems, *J. Geophys. Res., 101*, 27,187, 1996.

Volland, H. A semiempirical model of large-scale magnetospheric electric fields, *J. Geophys. Res., 78*, 171, 1973.

Weimer, D. R., A flexible, IMF dependent model of high-latitude electric potentials having "space weather" applications, *Geophys. Res. Lett., 23*, 2549, 1996.

Wolf, R. A., and R. W. Spiro, Numerical modeling of the ring current and plasmasphere, *Space Sci. Rev., 80*, 199, 1997.

Wu, C.-C., and R. P. Lepping, Effects of magnetic clouds on the occurrence of geomagnetic storms: The first 4 years of Wind, *J. Geophys. Res., 107*(A10), 1314, doi: 10.1029/2001JA000161, 2002.

Yeh, H.-C., J. C. Foster, F. J. Rich, and W. Swider, Storm time electric field penetration observed at mid-latitude, *J. Geophys. Res., 96*, 5707, 1991.
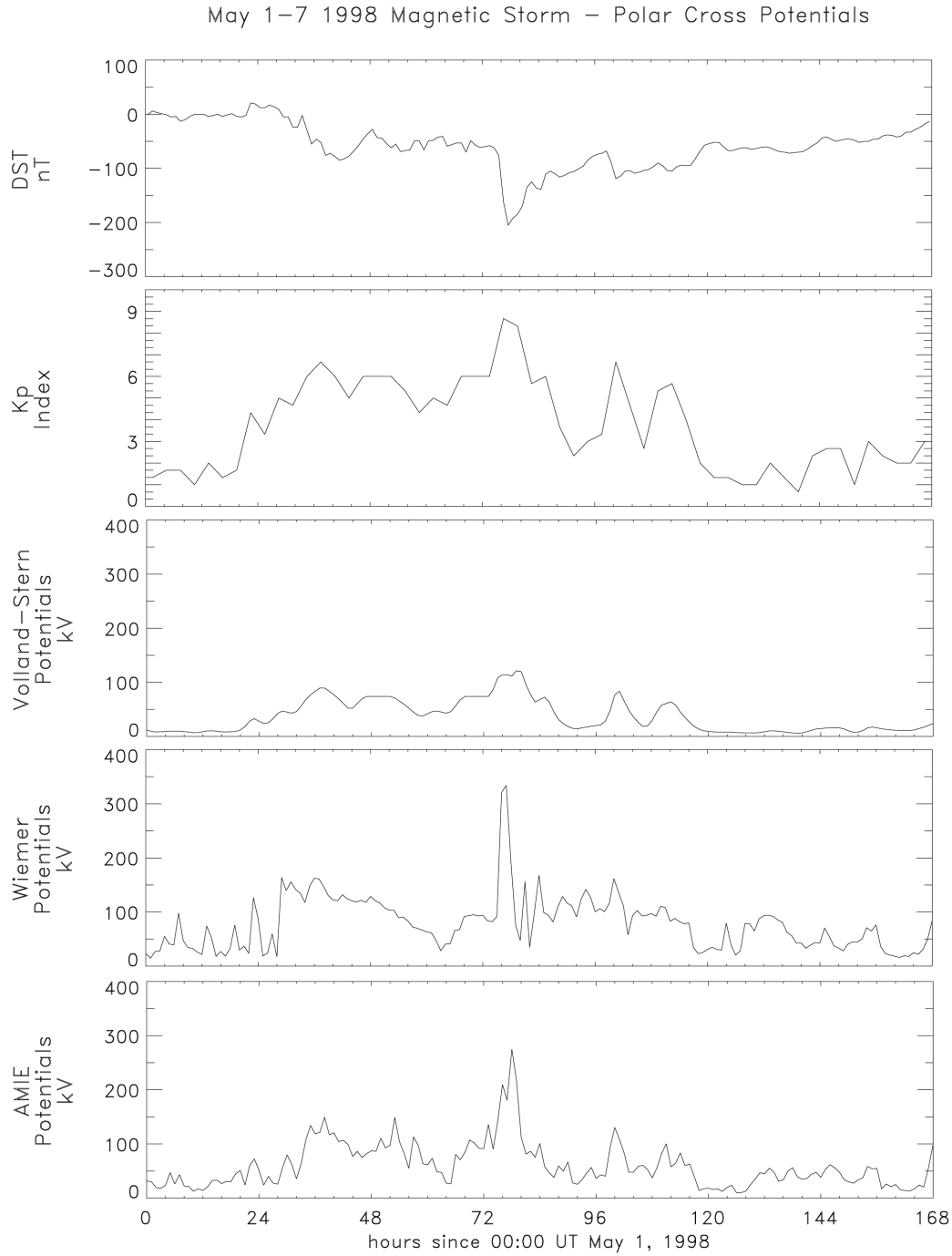
Figure 1. Geophysical quantitites during the 4 May 1998 magnetic storm. The first two rows are the Dst and Kp global indices. The next three panels show the total cross-tail potential differences during the 4 May 1998 storm from the Volland-Stern model, the Weimer-96 model, and the AMIE model.

25
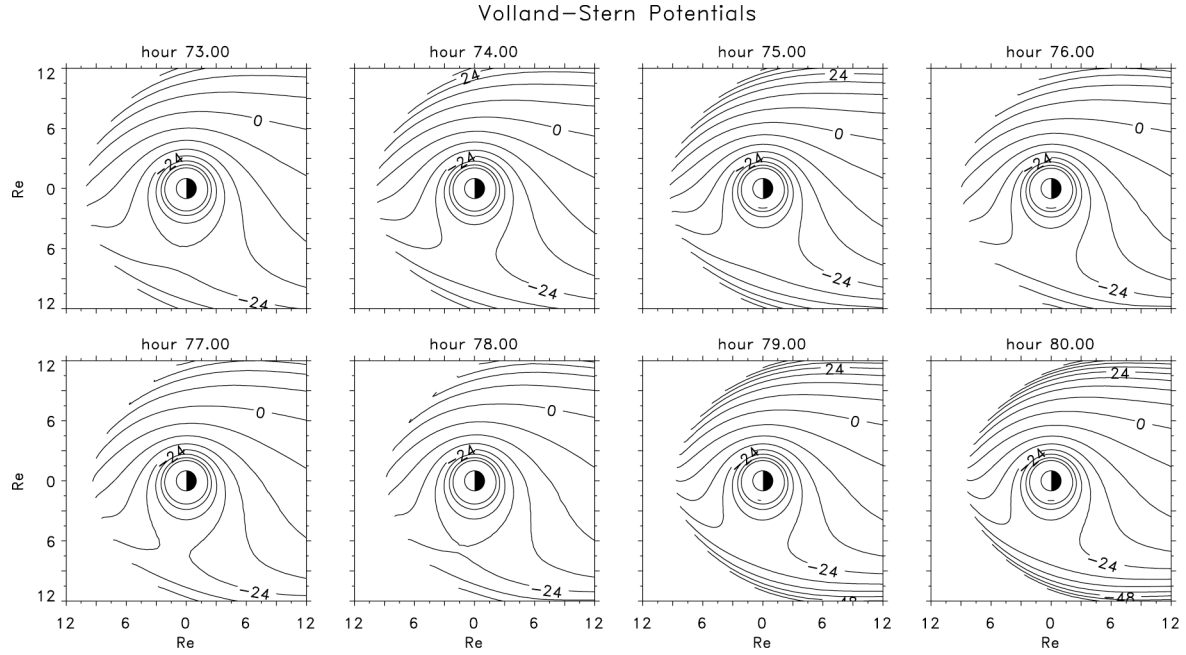
Figure 2

Figure 2. Electric potential isocontour plots for the Volland-Stern electric field model at 8 times during the main phase of the 4 May 1998 storm. Contours are shown every 6 kV, and are not drawn inside of 2 R_E or beyond the magnetopause, as specified in the model. Note that corotation is included in the potential pattern.

Figure 3
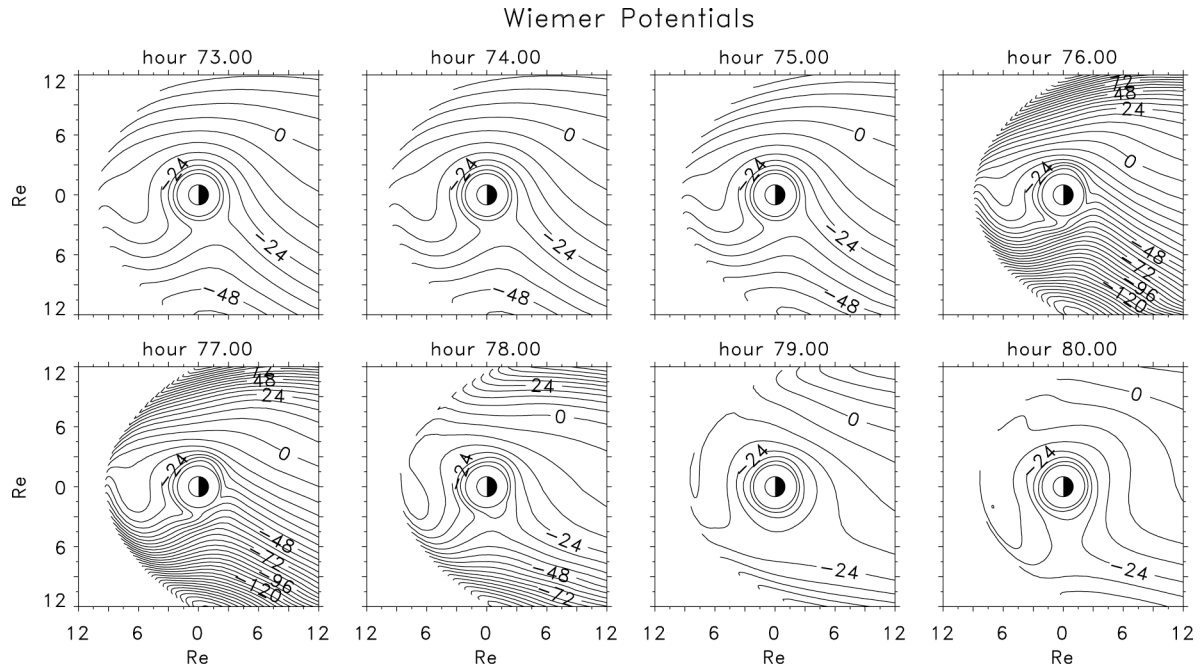
Figure 3. Electric potential isocontour plots like Figure 2, except for the Weimer-96 electric field model. Note that corotation is included in the potential pattern.

Figure 4
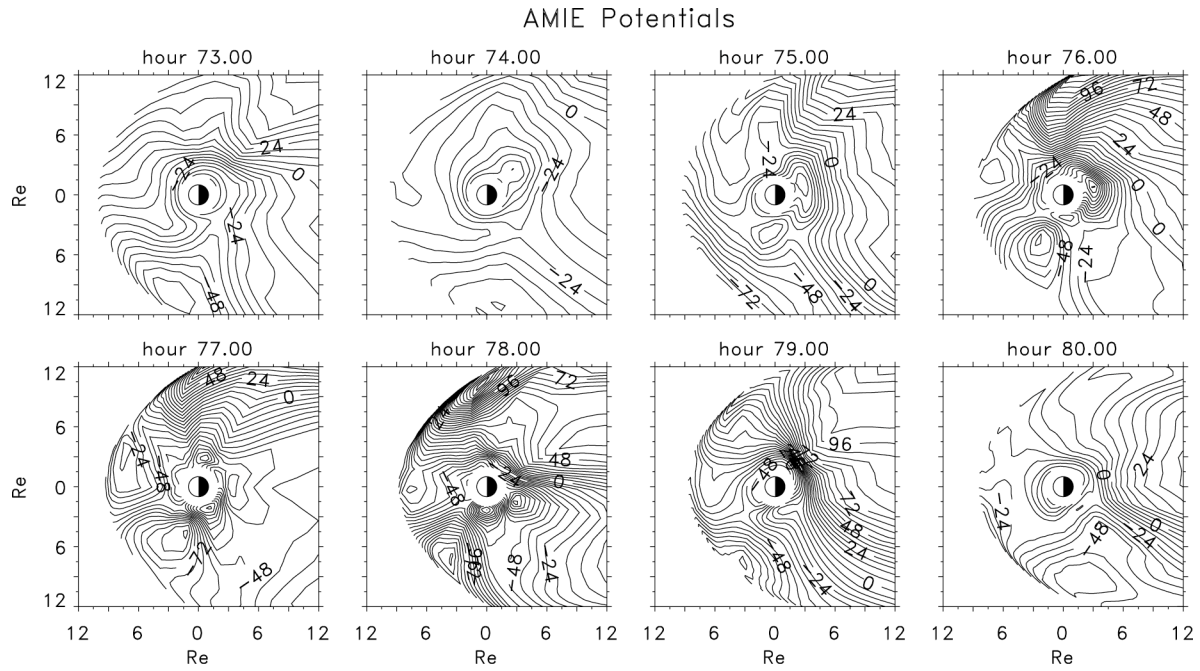
Figure 4. Electric potential isocontour plots like Figure 2, except for the AMIE electric field model. Note that corotation is included in the potential pattern.

Figure 5
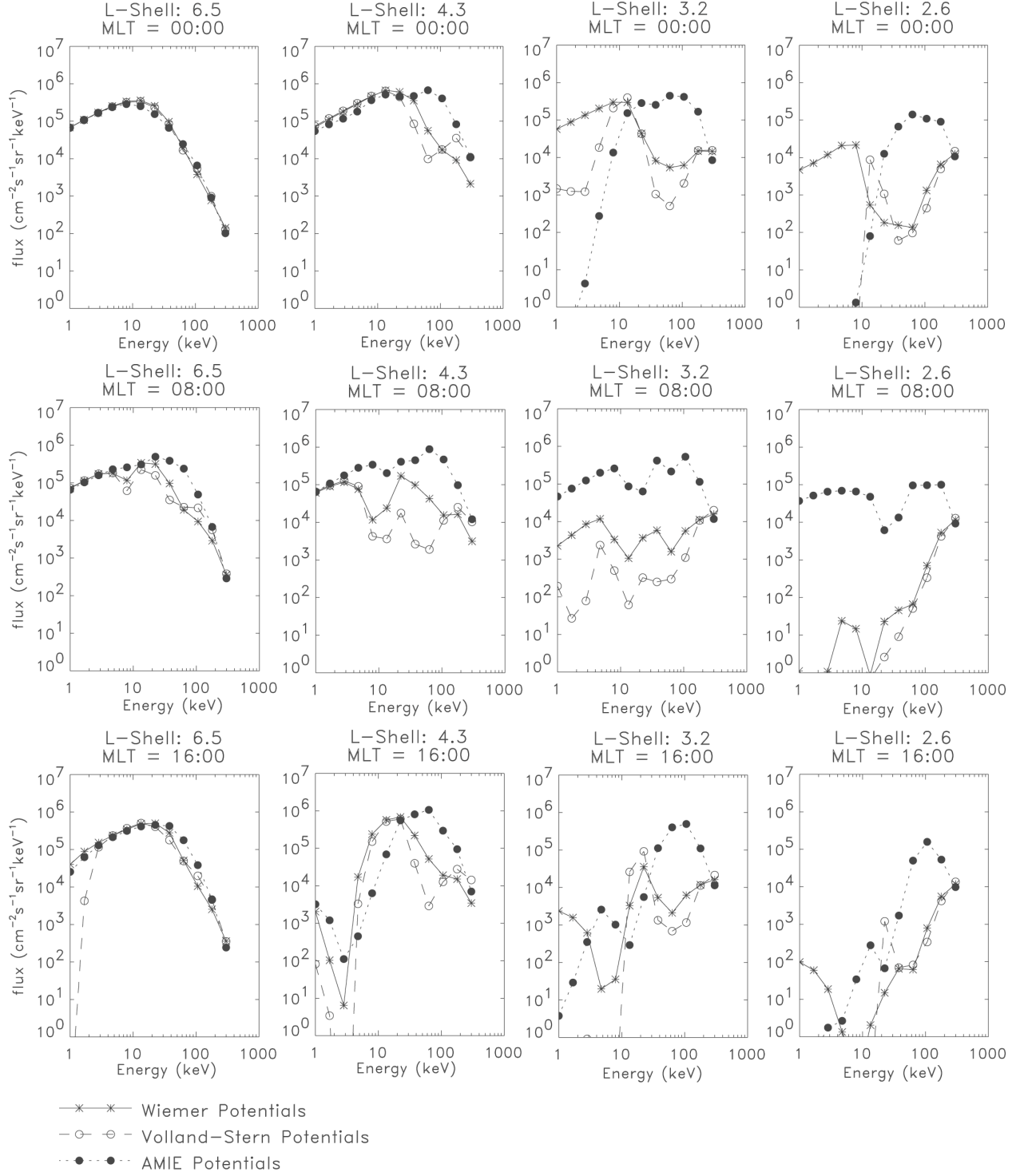
Figure 5. Pitch angle averaged number flux energy spectra of protons at hour 74 (02 UT, start of the main phase), shown at 3 local times (rows) and at 4 radial distances (columns).

Figure 6
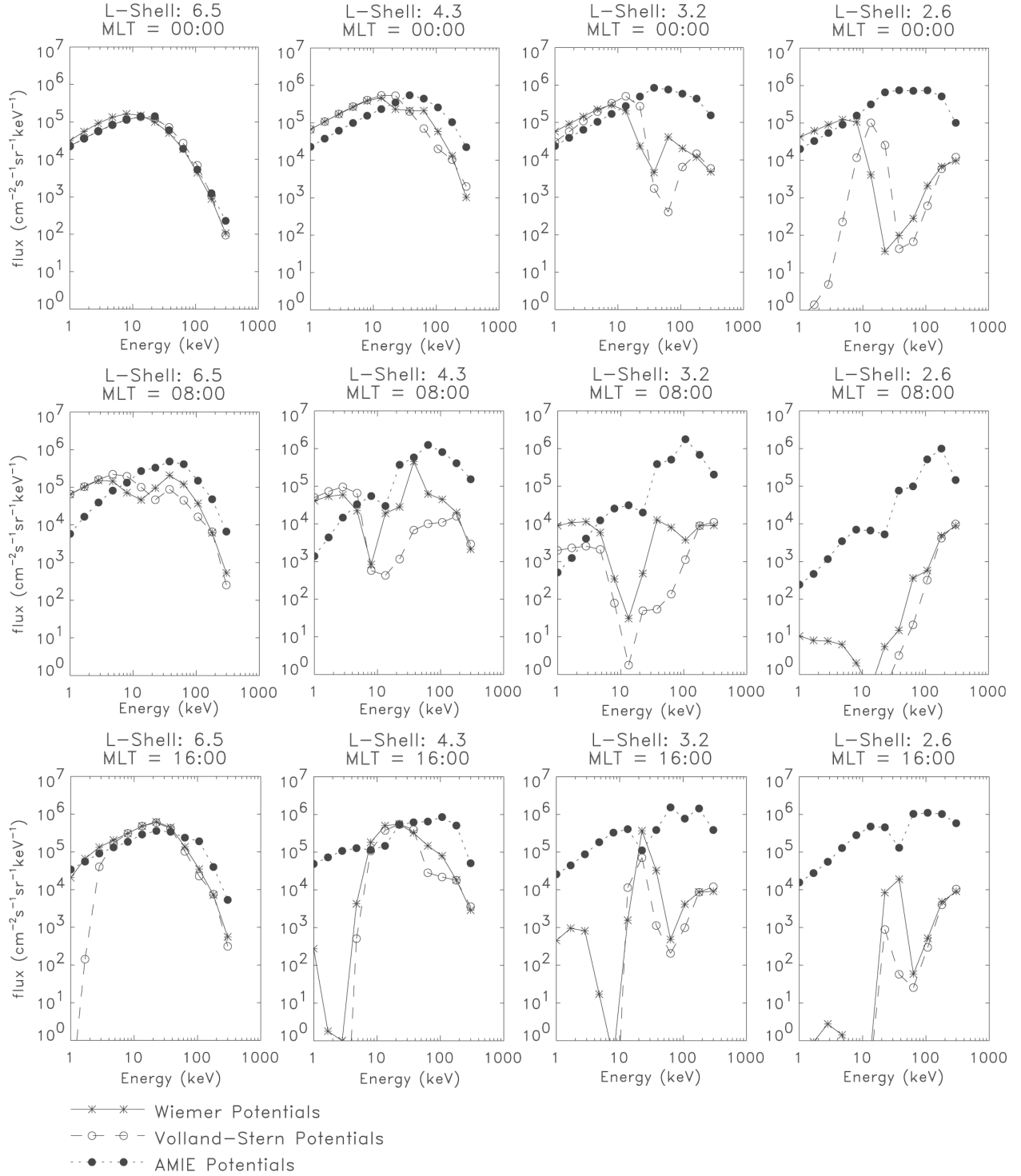
Figure 6. Same as Figure 5 except for protons at hour 80 (08 UT, end of the main phase).

Figure 7
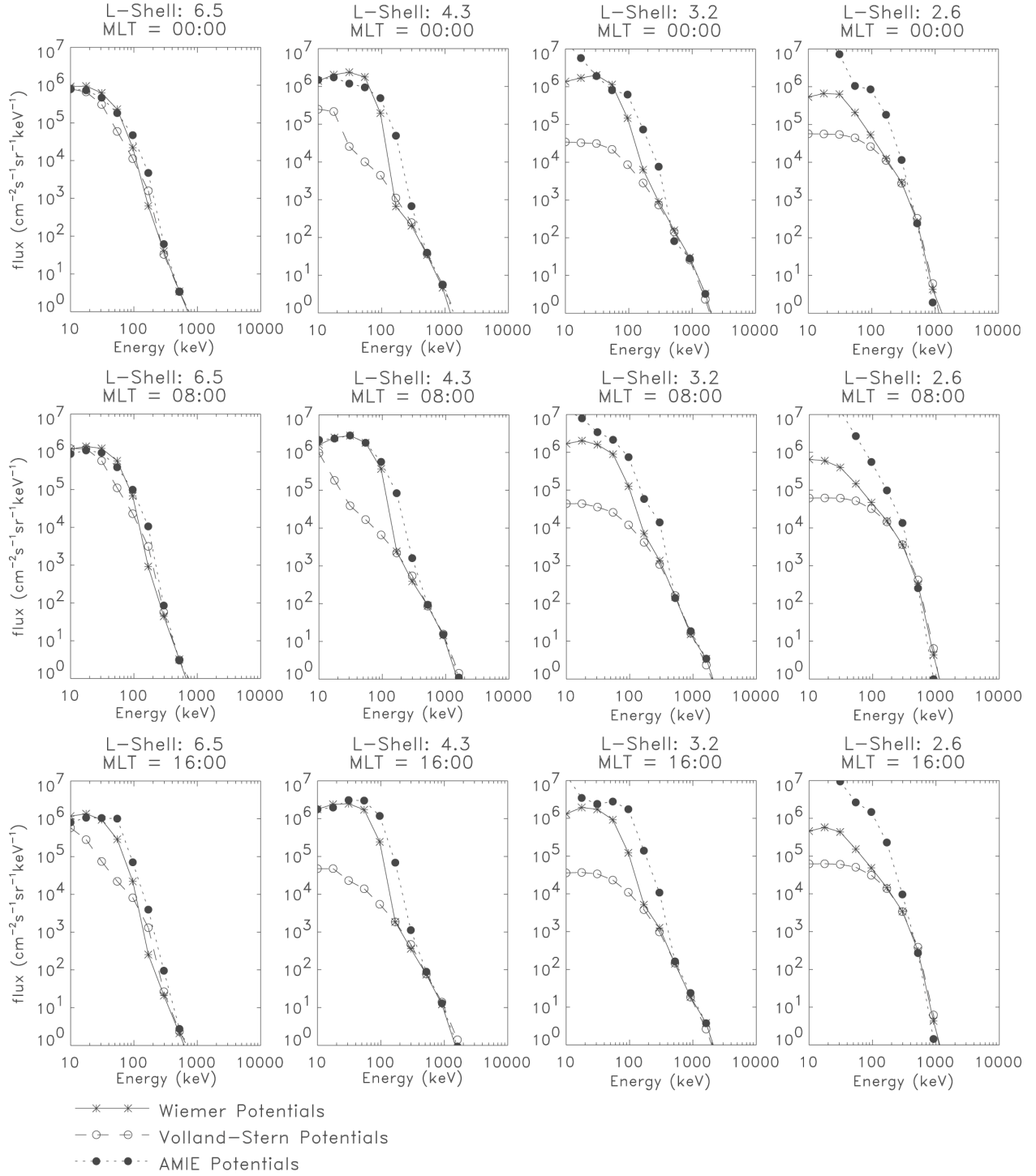
Figure 7. Same as Figure 5 except for electrons at hour 74 (02 UT, start of the main phase).
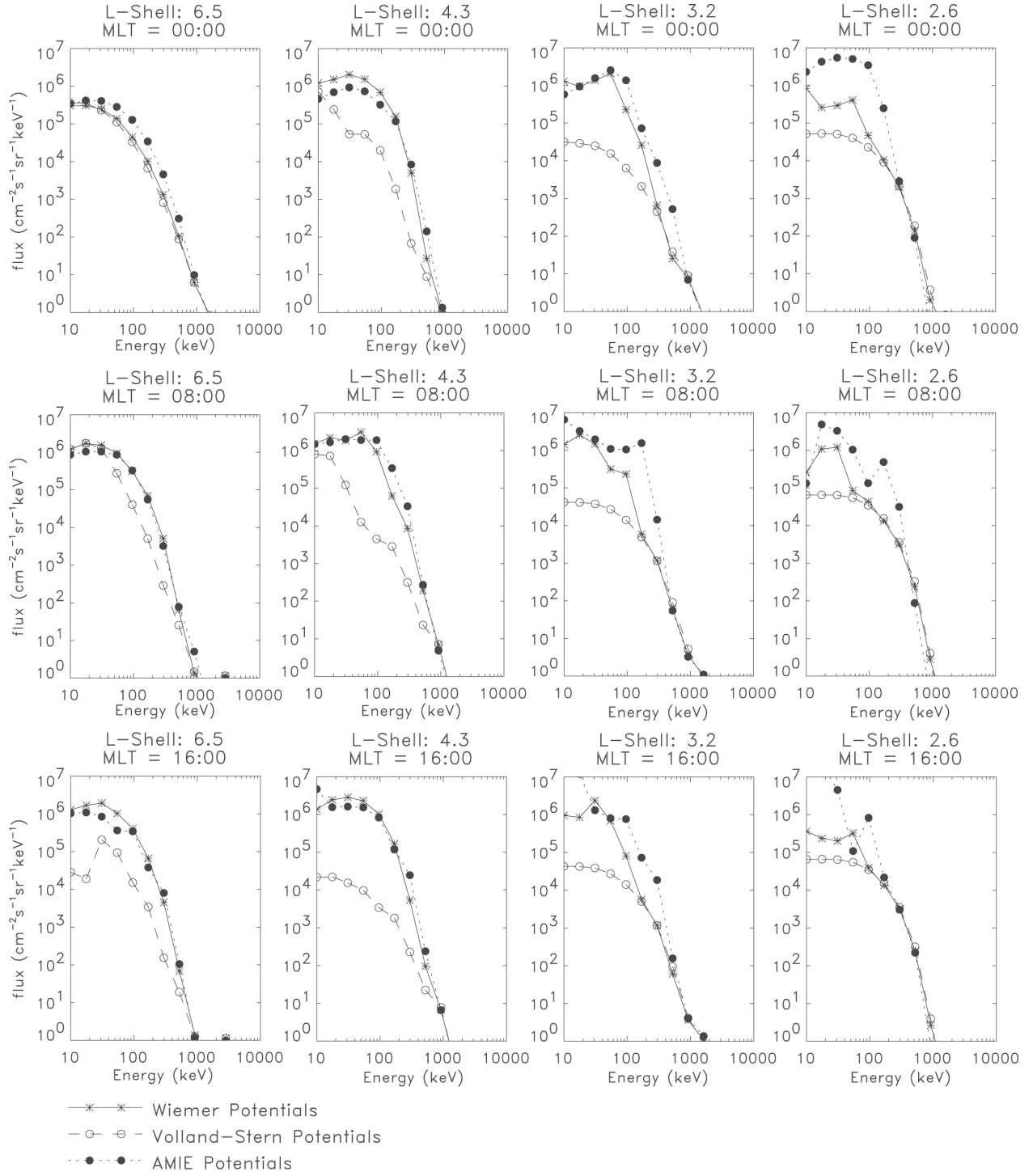
31

Figure 8

Figure 8. Same as Figure 5 except for electrons at hour 80 (08 UT, end of the main phase).
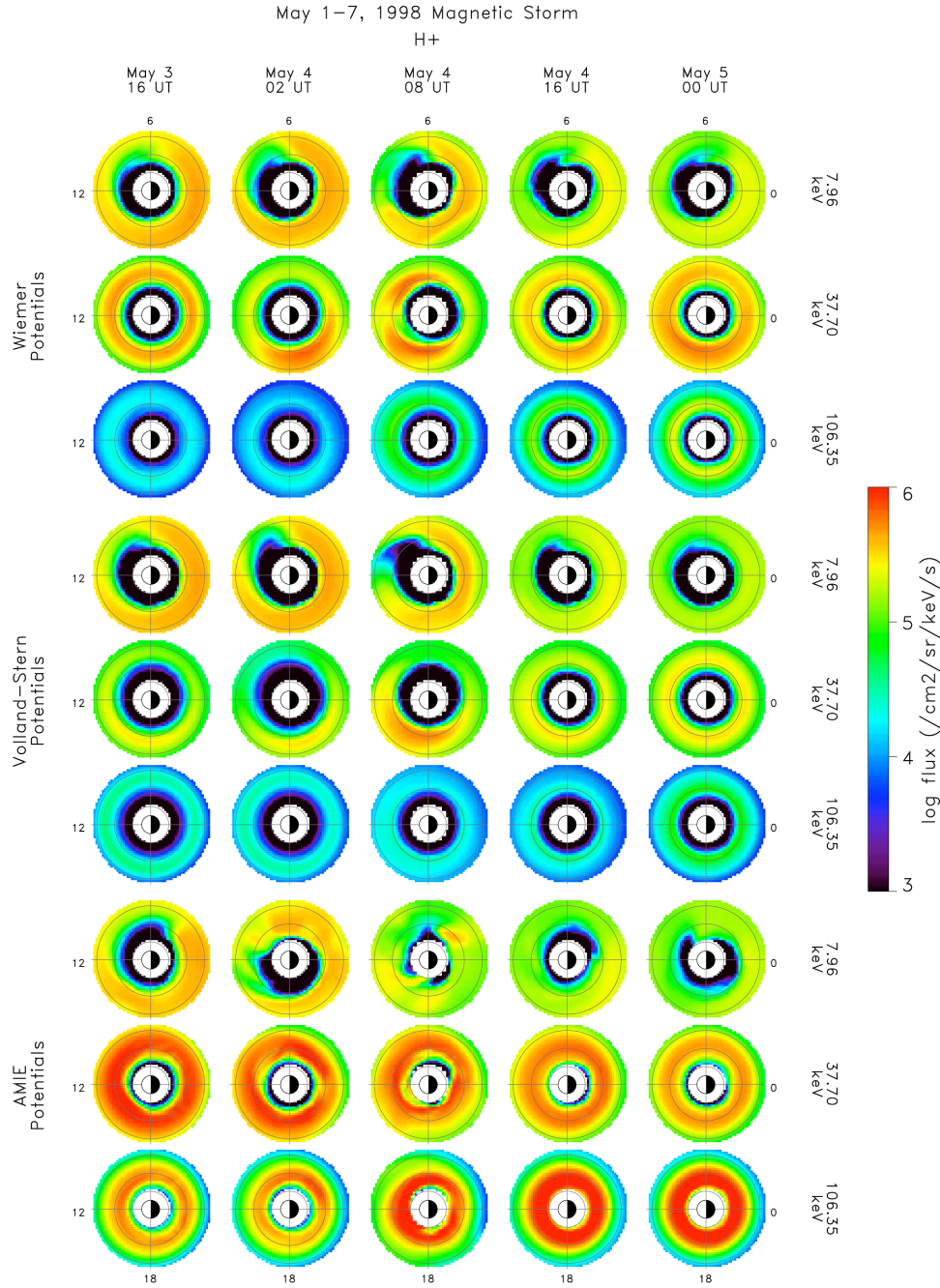
Figure 9

Figure 9. Pitch-angle averaged H$^+$ differential number flux at 5 times during the storm (columns). For each of the 3 electric potential descriptions (sets of rows), 3 energies are shown (rows in each set). Each plot extends to 6.6 R$_E$, with gray circles drawn every 2 R$_E$. Local noon is to the left and dawn is to the top in each plot.
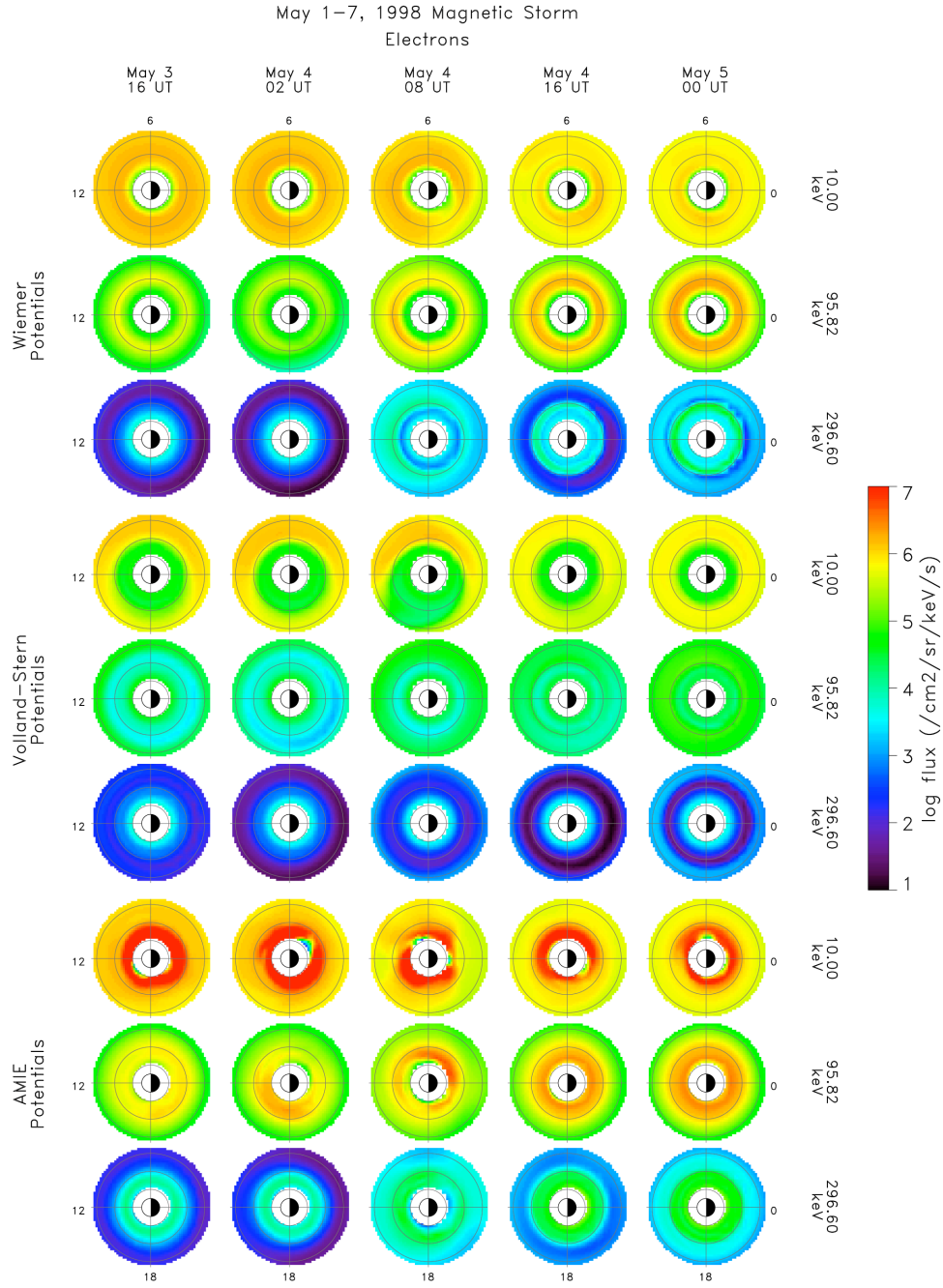
Figure 10

Figure 10. Same as Figure 9, except for electrons. Note that the selected energies are different than those chosen for the ion results.